JACS
JOURNAL OF THE AMERICAN CHEMICAL SOCIETY
pubs.acs.org/JACS
Article

Heterotrimetallic Precursor with 2:2:1 Metal Ratio Requiring at Least a Pentanuclear Molecular Assembly

Haixiang Han, Jesse C. Carozza, Zheng Zhou, Yuxuan Zhang, Zheng Wei, Artem M. Abakumov, Alexander S. Filatov, Yu-Sheng Chen, Daniel J. SantaLucia, John F. Berry, and Evgeny V. Dikarev*

Cite This: J. Am. Chem. Soc. 2020, 142, 12767−12776
Read Online
ACCESS | Metrics & More | Article Recommendations | Supporting Information

ABSTRACT: This work represents an important step in the quest to make heteromultimetallic molecules featuring specific metal types and complicated metal ratios. The rational design, synthesis, and characterization of a complex heterotrimetallic single-source molecular precursor for the next generation sodium-ion battery cathode material, $Na_2Mn_2FeO_6$, is described. A unique pentametallic platform $[Mn^{II}(ptac)_3{-}Na{-}Mn^{III}(acac)_3{-}Na{-}Mn^{II}(ptac)_3]$ (**1**) was derived from the known polymeric structure of $[NaMn^{II}(acac)_3]_\infty$, through a series of elaborate design procedures, such as mixed-ligand, unsymmetric ligand, and mixed-valent approaches. Importantly, the application of those techniques results in a molecule with distinctively different transition metal positions in terms of ligand environment and oxidation states. An isovalent substitution of Fe^{III} for the central Mn^{III} ion forms the target heterotrimetallic precursor $[Mn^{II}(ptac)_3{-}Na{-}Fe^{III}(acac)_3{-}Na{-}Mn^{II}(ptac)_3]$ (**3**) with an appropriate metal ratio of Na:Mn:Fe = 2:2:1. The arrangement of metal ions and ligands in this pentametallic assembly was confirmed by single crystal X-ray investigation. The unambiguous assignment of the positions and oxidation states of the Periodic Table neighbors Fe and Mn in **3** has been achieved by a combination of investigative techniques that include synchrotron resonant diffraction, X-ray multiwavelength anomalous diffraction, X-ray fluorescence spectroscopy, Mössbauer spectroscopy, and gas-phase DART mass spectrometry. The heterotrimetallic single-source precursor **3** was shown to exhibit a clean decomposition pattern yielding the phase-pure P2−$Na_2Mn_2FeO_6$ quaternary oxide with high uniformity of metal ion distribution as confirmed by electron microscopy.

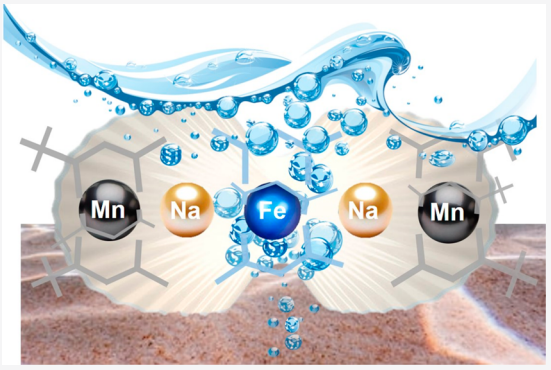

INTRODUCTION

Throughout the long history of functional materials development, transition metals have provided fertile ground for adjusting optical, electrochemical, magnetic, and catalytic characteristics of materials.[1−4] Naturally, the discovery of a simple prototype with a single active transition metal is followed by incorporation of a second or even third transition metal type, in order to further broaden structural variety as well as to achieve superior properties of interest.[5−7] Increasing compositional complexity often offers a diversity of microstructures to satisfy specific purposes. Additional transition metal(s) are known to interact with the primary active center, enhancing its desired characteristics and activities.[8] Moreover, combining multiple metal types in one compound allows for the rebalancing or even enrichment of beneficial properties and/or compensation for undesirable drawbacks, thus greatly expanding the scope of available new materials.[9,10] Importantly, the incorporation of multiple transition metals goes well beyond augmenting the existing properties brought on by the individual metal; instead, their synergistic cooperation can result in entirely new and unexpected phenomena.[11] Finally, the inclusion of additional metal types provides more tunable parameters (metal combinations, ratios, coordination number/environment), allowing for a greater adjustment of material characteristics based on specific needs.[12,13]

One particular area that benefits most from the trend of increasing the compositional complexity of materials is the development of improved electrode materials for Li/Na-ion batteries.[14−17] For example, addition of a second transition metal (Cr, Fe, Co, and Ni) to the famous $LiMn_2O_4$ spinel led to the discovery of the $LiMn_{2-x}M_xO_4$ class of materials that offers high working potentials above 5 V.[8,18] These quaternary oxides demonstrate a two-step charge/discharge process with the high-voltage component being attributed to the second transition metal, which also contributes to the increased stability of the electrode. An even more impressive example of synergistic interaction between transition metals is the

Received: May 10, 2020
Published: June 23, 2020

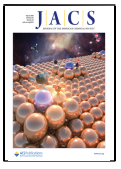

https://dx.doi.org/10.1021/jacs.0c05139
J. Am. Chem. Soc. 2020, 142, 12767−12776

currently popular family of Li NMC materials ($LiNi_{1-x-y}Mn_xCo_yO_2$) that were developed to overcome the drawbacks of the layered $LiNiO_2$ parent.[19,20] The addition of Co^{3+} reduces the amount of Ni^{2+} and improves the rate capability, Mn^{4+} stabilizes the structure and prevents phase transformations during cycling, while Ni^{2+}/Ni^{4+} still acts as an electrochemically active redox couple.[21]

Among the alkali ions, sodium has the most similar properties to lithium, with the added benefit of high abundance and low cost.[14,17] However, the larger size of sodium ions significantly restricts the number of suitable host structures with a single 3d transition metal for reversible de/intercalation.[22] That is why the introduction of additional transition metal(s) leads to dramatic expansion of the appropriate frameworks. The $NaFeO_2$ layered oxide was deemed as a promising cathode material for Na-ion batteries due to its simple structure, straightforward synthesis, natural abundance of its constituent elements, environmental benignity, and high operating voltage of the Fe^{3+}/Fe^{4+} redox couple.[23] However, it was found to suffer from numerous irreversible phase transitions during cycling, initiating the call for structural and compositional modifications. Partial substitution of Fe with other transition metals led to the discovery of P2-type $Na_{2/3}M_{2/3}M'_{1/3}O_2$ cathode materials that were found to prevent structural degradation while delivering a higher capacity.[12,14,24] Among this family of newly emerging Na-ion cathode materials, $Na_{2/3}Mn_{2/3}Fe_{1/3}O_2$ (or $Na_2Mn_2FeO_6$) appears to be the most promising as it demonstrates the highest discharge capacity along with a durable cycle life.[25,26]

Nevertheless, there are still a number of challenges for the efficient synthesis of quaternary oxides that contain two different 3*d* transition metals. The presence of more than one transition metal exponentially increases the difficulty in achieving homogeneous metal distribution within the bulk product and often results in a "pseudo-quaternary" oxide, which is, in fact, a mixture of distinct components with different metal constituents.[27] Furthermore, the presence of more metals opens up a variety of pathways for the formation of thermodynamically stable but undesired intermediates, especially binary and tertiary oxides.[28] One effective way to deal with the aforementioned problems is to employ a high-temperature annealing process in order to force all metals to uniformly disperse throughout the entire body of oxide.[29,30] However, this method often results in sintering of the particles into large aggregates, losing the novel properties originating from the nanostructured matrix. Notably, for multimetallic functional materials, the compositional complexity exerts certain limitations on application of advanced preparative techniques, such as chemical vapor deposition (CVD) or liquid injection, for growth of thin films with the proper morphology and stoichiometry.[31,32]

An effective way to solve the above-mentioned problems is the application of single-source precursors, molecules containing all of the required metals in a proper ratio and decomposable under mild conditions to yield the desired phase-pure materials.[33,34] Compared to the conventional high-temperature solid state synthetic route, this approach allows one to mix different metals at the molecular level, providing a rapid interaction between the constituent elements, ensuring homogeneous metal distribution in the bulk product, avoiding the formation of certain thermally stable, but unwanted intermediates, as well as offering a low-temperature pathway to the targeted nanostructured materials.[34] Despite significant progress that has been achieved in designing hetero*bi*metallic precursors with simple (e.g., 1:1 and 1:2) metal ratios, the development of suitable molecules still significantly lags behind the rapid evolution of complex functional materials. The preparation of hetero*tri*metallic precursors even with a primary 1:1:1 metal ratio is already quite challenging, especially when neighboring elements on the Periodic Table are involved.[35] The quest for more complex compositions requires the development of a new bag of tricks.

Herein we report the design, synthesis, and characterization of the hetero*tri*metallic, mixed-valent molecular precursor $[Mn^{II}(ptac)_3NaFe^{III}(acac)_3NaMn^{II}(ptac)_3]$ with a Na:Mn:Fe ratio of 2:2:1 (acac = pentane-2,4-dionate; ptac = 1,1,1-trifluoro-5,5-dimethyl-2,4-hexanedionate, Scheme 1). A one-pot, high-yield synthetic procedure was utilized to obtain the heterometallic complex from commercially/readily available starting reagents. By using a combination of characterization techniques, it was unambiguously confirmed that the pentanuclear molecule represents a "true" hetero*tri*metallic assembly with transition metal ions fully occupying their corresponding positions. Importantly, it was demonstrated that a hetero*tri*metallic precursor can be utilized in an efficient synthesis of the target prospective cathode material, $Na_2Mn_2FeO_6$.

Scheme 1. Schematic Presentation of the Ligands

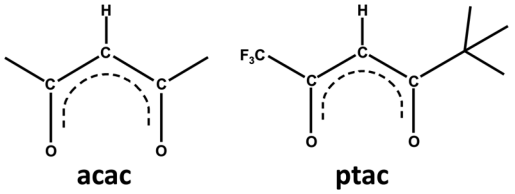

Design of the Hetero*tri*metallic Precursor. An obvious assumption for creating a single-source precursor for the target $Na_{2/3}Mn_{2/3}Fe_{1/3}O_2$ (or $Na_2Mn_2FeO_6$) oxide material is that it requires at least a pentanuclear core molecule accommodating the Na, Mn, and Fe metals in a 2:2:1 ratio. In addition, it should provide sufficient distinction (coordination, geometry) for the Mn and Fe positions, so that it represents a "true" hetero*tri*metallic rather than a statistical mixture of two hetero*bi*metallic molecules. The latter can be achieved by using different ligands and/or oxidation states for two neighboring transition metals. Furthermore, the ligands employed should assist in a clean, low-temperature decomposition of the hetero*tri*metallic precursor yielding the target phase-pure quaternary oxide. As might be expected, no appropriate pentametallic structure is known[36,37] that can serve as a precursor for the target 2:2:1 oxide material. These considerations forced us to look for some suitable hetero-*bi*metallic templates that could be effectively modified to complete the quest.

As a starting point for our conceptual design of a pentanuclear hetero*tri*metallic molecular precursor with the Na:Mn:Fe ratio of 2:2:1, the polymeric structure of $[NaMn^{II}(acac)_3]_\infty$ (Scheme 2a) was identified.[38] This structure type is known for a number of divalent 3d transition metals[39] and is represented by a 1-D infinite chain of alternating Na^+ and $[Mn(acac)_3]^-$ units. This arrangement is possible due to the sterically small Mn-chelating acac ligands

https://dx.doi.org/10.1021/jacs.0c05139
J. Am. Chem. Soc. 2020, 142, 12767−12776

Scheme 2. Conceptual Design of the Target Pentanuclear Heterotrimetallic Molecular Precursor

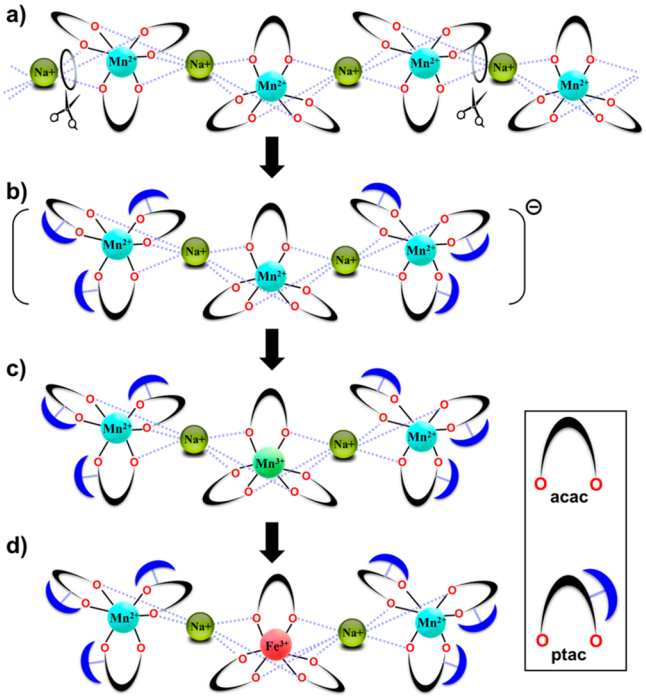

that are capable of using all six of their oxygen atoms to interact with sodium ions on both sides.

In the first step of a conceptual construction, in order to form a discrete pentanuclear assembly, we cut the polymeric chain (see scissors in Scheme 2a) by employing the unsymmetric ptac ligands in a 2:1 ratio to acac groups. The ptac ligand serves two purposes. (1) The first is to limit the chain length by preventing further agglomeration, since the ptac ligands' bulky ^{t}Bu substituents face outside of the pentanuclear assembly. The bulky ends are blocking (see the umbrellas in Scheme 2b) the corresponding proximal oxygen atoms from participating in bridging interactions with Na ions. Conversely, the oxygen atoms beneath the small trifluoromethyl groups can still coordinate to the Na^+ centers. (2) Utilization of the mixed-ligand approach allows one to induce a sufficiently different coordination environment for the central vs terminal metal ions. This results in the pentanuclear anionic fragment $[Mn^{II}(ptac)_3NaMn^{II}(acac)_3NaMn^{II}(ptac)_3]^-$ (Scheme 2b).

In order to make the pentanuclear assembly neutral and to insert even more distinction into the coordination environments of the inner and outer transition metal positions, we replace the central divalent ion with trivalent manganese, making the charge-neutral pentanuclear molecule $[Mn^{II}(ptac)_3NaMn^{III}(acac)_3NaMn^{II}(ptac)_3]$ (Scheme 2c). Importantly, in this mixed-valent approach, the electron-poorer trivalent center is now chelated by electron-donating acac groups, while the less electron-donating ptac ligands are coordinated to the more electron-rich divalent ions.

In the last step, by taking into account our previous observations that mixed-valent heterometallic diketonates overwhelmingly support the Fe^{3+}/Mn^{2+} couple,[40] we considered the isovalent substitution of Fe^{III} for the middle Mn^{III} ion, affording the heterotrimetallic precursor $[Mn^{II}(ptac)_3NaFe^{III}(acac)_3NaMn^{II}(ptac)_3]$ (Scheme 2d) with Na:Mn:Fe ratio of 2:2:1.

RESULTS AND DISCUSSION

Synthesis and Properties. The two parent heterobimetallic complexes $[Na_2Mn_3(acac)_3(ptac)_6]$ (**1**) and $[Na_2Fe_3(acac)_3(ptac)_6]$ (**2**) as well as the final target heterotrimetallic precursor $[Na_2Mn_2Fe(acac)_3(ptac)_6]$ (**3**) can be effectively prepared by a one-step reaction employing commercially/readily available starting reagents, performed either in the solid state or in solution with high yield (SI, Table S1):

$$6Na(ptac) + 2M^{II}Cl_2 + M'^{III}(acac)_3 \rightarrow Na_2M_2M'(acac)_3(ptac)_6 + 4NaCl \quad (1)$$

In the solid state approach, the reagents were sealed in an evacuated ampule and placed in a gradient furnace at 70 °C for 5−7 days, allowing the crystalline products to be deposited in the "cold" zone of the container, while the nonvolatile byproduct NaCl remained in the "hot" end. Complex **1** appears as brown crystals, while **2** and **3** are both orange. Overheating triggers decomposition of the products, yielding brown (**1**) or red (**2** and **3**) oily liquids that do not solidify upon cooling down the reaction mixture. Therefore, careful control of the reaction temperature is critical for the preparation of phase-pure products. In addition, the purity of the starting reagent, $M^{III}(acac)_3$ (M = Mn and Fe), was found to play a critical role in the formation of pentanuclear complexes. Compared with the solid state synthetic route, the preparation of precursors can be effectively scaled up by running the solution reaction in hexanes at room temperature. The white NaCl precipitate can be readily separated from products by filtration. Complexes **1**−**3** are stable in the open air for a long period of time, as confirmed by powder X-ray diffraction. Heterometallic precursors are all highly volatile at temperatures as low as 65 °C, readily soluble in all common solvents, and their thermal decompositions start at about 100 °C.

Single Crystal X-ray Investigation. Single crystal X-ray diffraction studies revealed the pentametallic structures (Figure 1 and SI, Figures S4 and S5) for heterobimetallic complexes $[M(ptac)_3NaM(acac)_3NaM(ptac)_3]$ (M = Mn (**1**) and Fe

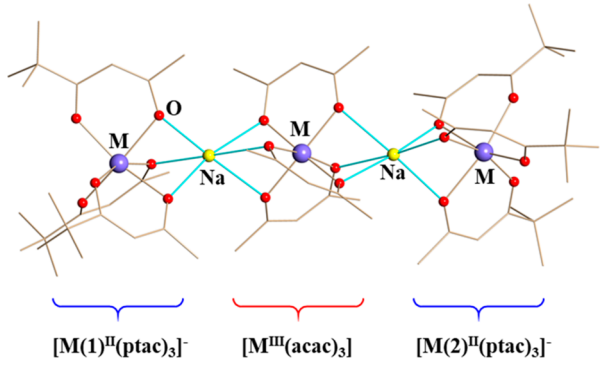

Figure 1. Single crystal structures of the heterobimetallic molecular complexes Δ,Δ,Δ-$[M(ptac)_3NaM(acac)_3NaM(ptac)_3]$ (M = Mn (**1**) and Fe (**2**)). The fluorine and hydrogen atoms are omitted for clarity. Full views of molecular structures **1** and **2** can be found in the SI, Figures S4 and S5.

https://dx.doi.org/10.1021/jacs.0c05139
J. Am. Chem. Soc. 2020, 142, 12767−12776

Table 1. Averaged M−O Bond Distances (Å) in Heterometallic Complexes[a]

	$[M^{II}(1)(ptac)_3]^-$	$[M^{III}(acac)_3]$	$[M^{II}(2)(ptac)_3]^-$
bond distances	$M^{II}(1)$−O	M^{III}−O	$M^{II}(2)$−O
Mn−Na−Mn−Na-Mn (**1**)	2.123, 2.179[b]	1.932 (2×), 2.021 (4×)	2.129, 2.184[b]
Fe−Na−Fe−Na-Fe (**2**)	2.074, 2.094[b]	1.995	2.068, 2.099[b]
Mn−Na−Fe−Na-Mn (**3**)	2.127, 2.179[b]	1.997	2.126, 2.180[b]

[a]Complexes **1**, **2**, and **3** are abbreviated as Mn−Na−Mn−Na-Mn, Fe−Na−Fe−Na-Fe, and Mn−Na−Fe−Na-Mn, respectively. The full list of the bond distances and angles can be found in the SI, Tables S7−S9. [b]M−O bond distance with oxygen atoms involved in bridging interactions.

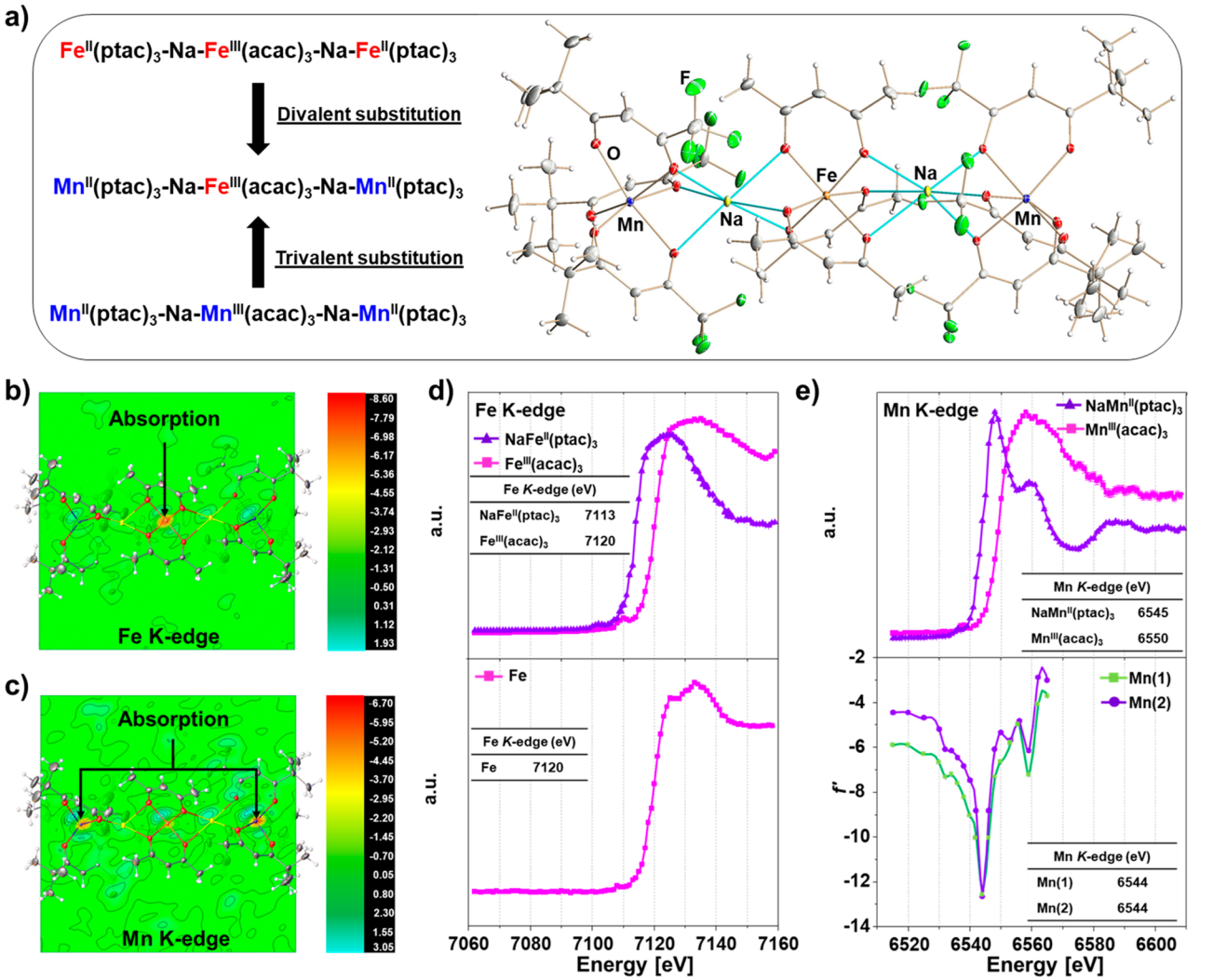

Figure 2. (a) Conceptual development of the hetero*tri*metallic precursor **3** from the parent hetero*bi*metallic models **1** and **2** (left) and molecular structure of pentanuclear complex $[Mn(ptac)_3NaFe(acac)_3NaMn(ptac)_3]$ (**3**, Δ,Δ,Δ-enantiomer) drawn with thermal ellipsoids at the 40% probability level (right). Difference Fourier electron density maps at absorption *K*-edges of Fe (b) and Mn (c) for the single crystal structure of **3**. (d) X-ray fluorescence scans collected in steps of 1 eV at 100 K around the Fe *K*-edge on the single crystals of $[NaFe^{II}(ptac)_3]$ (violet) and $[Fe^{III}(acac)_3]$ (magenta; top) compared with that of the Fe position in the structure **3** (bottom). (e) X-ray fluorescence scans collected in steps of 1 eV at 100 K around the Mn *K*-edge on the single crystals of $[NaMn^{II}(ptac)_3]$ (violet) and $[Mn^{III}(acac)_3]$ (magenta; top) compared with the anomalous scattering factor *f*′ plots of two Mn positions (bottom) in the structure **3**.

(**2**)). The structures are isomorphous and crystallize in the centrosymmetric triclinic space group $P\bar{1}$ with two molecules in the unit cell represented by Λ,Λ,Λ- and Δ,Δ,Δ-enantiomers. All three transition metals in each molecule are *tris*-chelated by diketonate ligands, with $[M(acac)_3]$ being in the middle and two $[M(ptac)_3]$ parts located at both termini of the pentanuclear assembly. These units are bridged by two "naked" sodium centers that exhibit a distorted octahedral coordination of diketonate oxygen atoms that chelate transition metal ions. The sterically uncongested acac groups in the middle of the heterometallic assembly use all six of their diketonate oxygen atoms for bridging interactions, while in the $[M(ptac)_3]$ end-units only the three oxygen atoms located under the proximal small CF_3 substituents are involved in coordination to sodium ions. The bulky ^{t}Bu tails of the ptac ligands face outward of the heterometallic assembly on both sides of the molecule and effectively prevent further aggregation and chain growth.

https://dx.doi.org/10.1021/jacs.0c05139
J. Am. Chem. Soc. 2020, 142, 12767−12776

Analysis of the M−O distances in the mixed-valent pentanuclear structures **1** and **2** (Table 1 and SI, Table S11) facilitates the assignment of the oxidation states of transition metal ions involved. Thus, the Fe−O bond distances in the $[Fe(acac)_3]$ part of **2** are practically the same as those in the monomeric $[Fe^{III}(acac)_3]$ (1.995 vs 2.000 Å),[41] while significantly shorter than those in the $[Fe^{II}(acac)_3]^-$ anionic fragment (2.070 Å),[42] clearly confirming the trivalent oxidation state for the central iron. On the other hand, the Fe−O bonds in both $[Fe(ptac)_3]$ fragments are longer than in the trivalent $[Fe^{III}(ptac)_3]$ complex (2.084 Å vs 1.991 Å)[43] but comparable to those in the $[Fe^{II}(\beta\text{-dik})_3]^-$ anionic fragments.[22] Similar consideration can be applied for the assignment of oxidation states of Mn ions in the molecule **1**. Additional evidence is provided by an apparent compressed Jahn−Teller effect in the central $[Mn(acac)_3]$ fragment that is characteristic of trivalent manganese and is always observed in the $[Mn^{III}(\beta\text{-dik})_3]$ complexes[44−46] (also see the molecular structure of $Mn(acac)_3$ in the SI, Figure S7 and Table S10). The above analysis points to the formulation of mixed-valent pentanuclear complexes **1** and **2** as $\{[M^{II}(ptac)_3]^-\text{-}Na^+\text{-}[M^{III}(acac)_3]\text{-}Na^+\text{-}[M^{II}(ptac)_3]^-\}$. Such an assignment fully supports our initial design strategy that places small, electron-donating acac ligands on the electron-poorer trivalent ion in the middle, while positioning unsymmetric, partially electron-withdrawing ptac groups to chelate the electron-richer divalent metal sites on both ends of heterometallic assembly.

Upon assigning the oxidation states for the Mn and Fe ions in the parent molecules **1** and **2**, we moved to decoding the transition metal positions in the hetero*tri*metallic complex **3** (Figure 2a and SI, Figure S6). As expected, the refinement of two Mn and one Fe at different atomic sites of the structure **3** did not reveal any significant differences. However, the correct assignments of 3d transition metal positions and oxidation states in hetero*tri*metallic molecule **3** can be achieved by comparing the M−O bond distances with those in the two parent bimetallic analogs **1** and **2** (Table 1 and SI, Table S11).

The central $[M(acac)_3]$ fragment in **3** appears to be essentially the same as the $[Fe^{III}(acac)_3]$ in complex **2** and lacks any Jahn−Teller distortion for the six M−O bonds seen in trivalent $[Mn^{III}(acac)_3]$ (SI, Figure S7 and Table S10). On the other hand, the two $[M(ptac)_3]$ side units are very similar to the corresponding $[Mn^{II}(ptac)_3]^-$ parts in **1** with essentially longer M−O bonds than those in the iron complex **2**. Based on the above considerations, we formulate hetero*tri*metallic complex **3** as $\{[Mn^{II}(ptac)_3]^-\text{-}Na^+\text{-}[Fe^{III}(acac)_3]\text{-}Na^+\text{-}[Mn^{II}(ptac)_3]^-\}$.

It is worth mentioning here that the preference for the Fe^{III}/Mn^{II} couple has already been observed in heterometallic diketonate structures.[40] Importantly, our attempts to synthesize the Mn^{III}/Fe^{II} "valent isomer" resulted in eventual redox/ligand exchange processes and formation of a mixture of **3** and **2**:

$$\begin{aligned} &2Mn(acac)_3 + 4FeCl_2 + 12Na(ptac) \\ &\rightarrow [Mn(ptac)_3\text{-}Na\text{-}Fe(acac)_3\text{-}Na\text{-}Mn(ptac)_3] \\ &\quad + [Fe(ptac)_3\text{-}Na\text{-}Fe(acac)_3\text{-}Na\text{-}Fe(ptac)_3] + 8NaCl \end{aligned} \quad (2)$$

X-ray Resonant Diffraction. The unique pentanuclear molecule **3** demonstrates a great structural complexity with three metal types presumably in different oxidation states (Na^+, M^{2+}, and M'^{3+}) and with three positions occupied by Periodic Table neighbors. As we have already learned from the structures of hetero*bi*metallic parents **1** and **2**, any of those positions can be occupied by Fe and Mn. Complicating matters is the fact that Mn and Fe have similar X-ray scattering factors. One should check if these sites have a mixed occupancy, which ultimately brings up the question if complex **3** represents a truly hetero*tri*metallic molecule (single-source precursor) or a mixture of hetero*bi*- and *tri*metallic counterparts (multi-source precursor). In order to distinguish neighboring elements on the Periodic Table having the same coordination number and similar environments, we employed X-ray resonant diffraction, an advanced technique that is capable of effectively distinguishing elements with very close atomic numbers based on significant differences in their anomalous dispersion factors at the specific absorption edges.[47] It has been utilized to provide an assignment of transition metal positions as well as to calculate the occupancy factors in hetero*tri*metallic molecule **3** that was initially formulated as $[Mn(ptac)_3NaFe(acac)_3NaMn(ptac)_3]$. The anomalous difference Fourier electron density maps at the wavelengths corresponding to the distinctive *K*-edges for Fe and Mn (7112 vs 6539 eV) display deep absorption at the central *tris*-acac chelated central unit and at *tris*-ptac chelated side-units, respectively (Figures 2b and 2c). Further refinement gives site occupancy factors as 0.989(1) for Fe in the $[Fe(acac)_3]$ fragment and 0.994(1)/0.996(1) for Mn in the two $[Mn(ptac)_3]$ parts (see SI for additional details). The results undoubtedly validate the assignment of the 3*d* transition metal positions in the pentanuclear assembly **3** and offer firm evidence for the presence of a "true" hetero*tri*metallic molecule.

X-ray Fluorescence and Multiple-Wavelength Anomalous Diffraction. Accurate assignment of transition metal oxidation states in heterometallic mixed-valent complexes is not only important for full characterization, but is instrumental in further engineering of this particular class of compounds via the isovalent substitution approach. Once the "true" hetero*tri*metallic nature of pentanuclear complex $[Mn(ptac)_3NaFe(acac)_3NaMn(ptac)_3]$ (**3**) has been established in resonant diffraction experiments, we applied other advanced synchrotron radiation techniques for analysis of the oxidation states of the Fe and Mn ions. X-ray fluorescence spectroscopy (see the SI for more information) was carried out in order to determine the oxidation state of the Fe ion (Figure 2d). Complex **3** was found to exhibit the same Fe *K*-edge energy (7220 eV) as the trivalent standard $[Fe^{III}(acac)_3]$, while being distinctively different from the divalent one $[NaFe^{II}(ptac)_3]$ (7113 eV), confirming the presence of Fe^{III} in the hetero*tri*metallic assembly **3** (SI, Figure S8). Taking into account that the two manganese ions in pentanuclear molecule **3** occupy crystallographically independent sites, it requires an assessment of each Mn position separately, which is beyond the capability of regular X-ray absorption/emission spectroscopy. Therefore, synchrotron X-ray multiple-wavelength anomalous diffraction (MAD) measurements have been carried out (see the SI for more information). This technique is based on the fact that the variation in the atomic scattering factor's (f') in-phase and out-of-phase components of the anomalous scattering function is sensitive to the near-edge wavelength employed. Refinement of f' for two individual resonating Mn ions at different wavelengths affords a clear plot of f' against energy for each position (SI, Table S12), from

https://dx.doi.org/10.1021/jacs.0c05139
J. Am. Chem. Soc. 2020, 142, 12767−12776

which the accurate *K*-edge number can be effectively identified as the energy corresponding to the minimum value of f'. As shown in Figure 2e, the two *tris*-ptac chelated Mn ions in $[Mn(ptac)_3]$ fragments demonstrate an identical *K*-edge energy of 6544 eV, indicating the same oxidation states for both. In addition, the Mn *K*-edge values for complex **3** are well aligned with the divalent $[NaMn^{II}(ptac)_3]$ standard (6545 eV) but significantly lower than that for the "more oxidized" $[Mn^{III}(acac)_3]$ (6550 eV; SI, Figure S9). Overall, the X-ray fluorescence and MAD investigations unambiguously support the assignment of the transition metal oxidation states in **3** as $\{[Mn^{II}(ptac)_3]^-$-Na^+-$[Fe^{III}(acac)_3]$-Na^+-$[Mn^{II}(ptac)_3]^-\}$.

Mössbauer Spectroscopy. Mössbauer spectroscopy allows one to sensitively examine the changes in the energy levels of an atomic nucleus in response to its oxidation states and environment. In this work, the Mössbauer spectra for the heterometallic complexes $[Fe(ptac)_3NaFe(acac)_3NaFe(ptac)_3]$ (**2**) and $[Mn(ptac)_3NaFe(acac)_3NaMn(ptac)_3]$ (**3**) were obtained at 294 K in order to confirm the oxidation states for the Fe ions in each structure.

In the spectrum of complex **2**, a fit for the data where the relative areas of each signal were fixed according to the expected 2:1 ratio of each type of Fe in $[Fe(ptac)_3NaFe(acac)_3NaFe(ptac)_3]$ is shown in Figure 3 (a second fit for the data where the areas for each signal were allowed to be freely refined is included in the SI, Figure S16). The relative area of the major signal was fixed to 0.667 and the one of the minor signal to 0.333. The other fitting parameters (see the SI for more details) were allowed to refine freely. This led to a fit with a reduced χ^2 value of 0.654. The major quadrupole doublet signal has an isomer shift of 1.154 mm/s and a quadrupole splitting of 2.314 mm/s. The minor quadrupole doublet signal shows an isomer shift of 0.360 mm/s and a quadrupole splitting of 0.619 mm/s. The fit to the data indicates two nonequivalent iron environments in the sample and corresponds well to the structure of complex **2**. The isomer shift and quadrupole splitting of the major signal are consistent with a high-spin divalent iron, while the isomer shift and quadrupole splitting for the minor signal are in agreement with a high-spin trivalent iron.

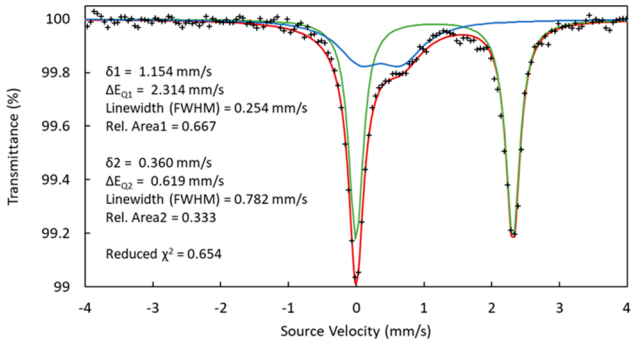

Figure 3. Room temperature Mössbauer spectrum of hetero*bi*metallic complex $[Fe(ptac)_3NaFe(acac)_3NaFe(ptac)_3]$ (**2**) with parameters from the fit. The data are displayed as black plus signs, the fit to the data as the red line, and the two quadrupole doublets comprising the fit are in green and blue.

The Mössbauer spectrum of the hetero*tri*metallic complex $[Mn(ptac)_3NaFe(acac)_3NaMn(ptac)_3]$ (**3**) is shown in Figure 4. The fit to the data yielded a similar isomer shift and quadrupole splitting to the minor signal as in the complex **2**.

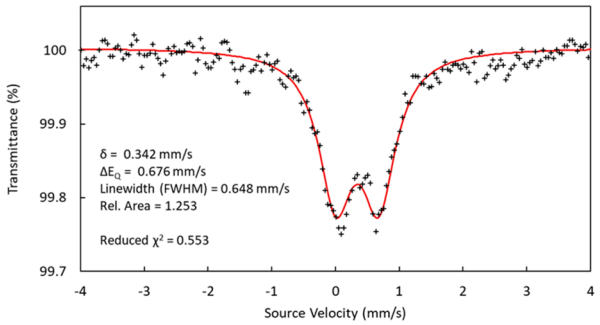

Figure 4. Room temperature Mössbauer spectrum of complex $[Mn^{II}(ptac)_3NaFe^{III}(acac)_3NaMn^{II}(ptac)_3]$ (**3**) with parameters from the fit. The data are displayed as black plus signs and the fit to the data as the red line.

The isomer shift was 0.342 mm/s, the quadrupole splitting was 0.676 mm/s, and the reduced χ^2 value for the fit was 0.553. It should be noted that, due to the poor signal-to-noise ratio from the obtained spectrum, the fit to the data seems to be heavily influenced by outlier points in the data. The parameter for the obtained isomer shift fits the experimental data well, while the quadrupole splitting parameter seems to be slightly overestimated when comparing the peak maxima in the fit and the peak maxima in the data. Nonetheless, the data are unambiguously interpreted as being consistent with a high-spin iron(III) center, which is expected given the similarity of the chemical environment of the Fe ion in **3** to that of the central Fe in complex **2**.

DART Mass Spectrometry Investigation of Hetero-*tri*metallic Complex 3. Direct Analysis in Real Time (DART) mass spectrometry has been successfully utilized to confirm the composition of complex heterometallic ions through their isotope distribution patterns[27,42,48] as well as to analyze the oxidation states of constituent transition metals.[49] In the positive-mode mass spectrum of solid $[Mn(ptac)_3NaFe(acac)_3NaMn(ptac)_3]$ (**3**), the peak corresponding to the $[M-L]^+$ (L = ptac; meas/calcd m/z = 1484.2365/1484.2410) ion appears with a characteristic isotope distribution pattern in good agreement with the simulated one (Figure 5a and SI, Figure S15 and Tables S17 and S18) confirming the presence

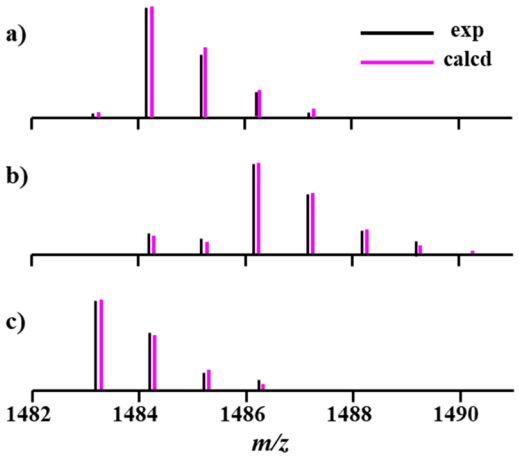

Figure 5. Isotope distribution patterns for the $[M\text{-ptac}]^+$ (M = $[Na_2M_2M'(ptac)_6(acac)_3]$) ions in the mass spectra of heterometallic complexes **3** (a), **2** (b), and **1** (c). Black and magenta lines represent experimental and calculated patterns, respectively.

https://dx.doi.org/10.1021/jacs.0c05139
J. Am. Chem. Soc. 2020, 142, 12767−12776

of pentanuclear hetero*tri*metallic [Na_2Mn_2Fe] species in the gas phase. Importantly, the isotope distribution pattern is clearly different from those of the parent hetero*bi*metallic [Na_2Fe_3] (**2**) and [Na_2Mn_3] (**1**) ions (Figure 5b,c and SI, Figures S13 and S14 and Tables S13−S16).

Careful analysis of fragment ions was found to provide critical information on the oxidation states of the transition metals in the hetero*tri*metallic complex **3**. Positive mode mass spectra of solid [$Mn^{II}(ptac)_3NaFe^{III}(acac)_3NaMn^{II}(ptac)_3$] (**3**) feature several ions (Figure 6a and SI, Table S17) that

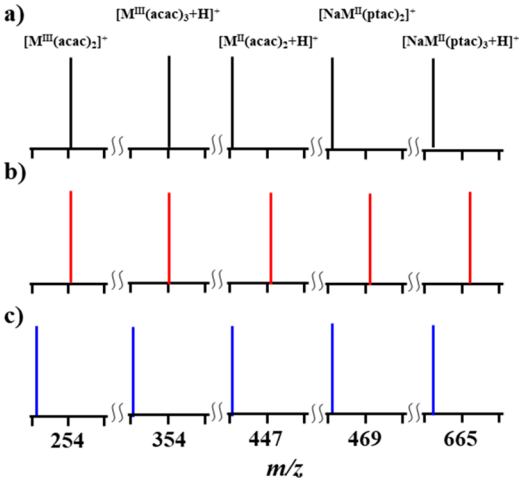

Figure 6. Characteristic mono- and dinuclear trivalent and divalent ions in the positive-ion DART mass spectra of heterometallic complexes **3** (a), **2** (b), and **1** (c).

correspond to trivalent iron ([$Fe^{III}(acac)_2$]$^+$ and [$Fe^{III}(acac)_3$+H]$^+$) and divalent manganese ([$Mn^{II}(acac)_2$+H]$^+$, [$NaMn^{II}(ptac)_2$]$^+$, and [$NaMn^{II}(ptac)_3$+H]$^+$), whereas any Fe^{II} and Mn^{III}-based peaks are absent. At the same time, the Fe^{II} and Mn^{III} peaks instantly appear in the spectra of hetero*bi*metallic [$Fe^{II}(ptac)_3NaFe^{III}(acac)_3NaFe^{II}(ptac)_3$] (**2**) (Figure 6b and SI, Figure S15) and [$Mn^{II}(ptac)_3NaMn^{III}(acac)_3NaMn^{II}(ptac)_3$] (**1**) (Figure 6c and SI, Figure S13).

Thermal Decomposition of Hetero*tri*metallic Precursor to Yield the Target Cathode Material. Thermal decomposition of hetero*tri*metallic precursor **3** was carried out in order to test its applicability for the preparation of the target quaternary oxide, which is an emerging cathode material of sodium ion batteries.[50,51] Pyrolysis of **3** in the air has been found to be a complex multistep process by thermogravimetric analysis (SI, Figure S17a). Decomposition starts around 100 °C and yields the $Na_{2/3}Mn_{2/3}Fe_{1/3}O_2$ oxide with poor crystallinity at around 400−450 °C. The residue continues to lose the mass, which was determined as the loss of Na in a form of Na_2O_2. Such changes in the sodium content are typically observed for this and similar types of sodium-transition metal oxides.[50,51] Increasing the temperature to 600 °C provides crystalline residue identified by X-ray powder diffraction as phase pure P2−$Na_xMn_{2/3}Fe_{1/3}O_2$ (SI, Figures S18 and S19). Further increase of the decomposition temperature simply improves the crystallinity of the oxide material, up to 750 °C, when side products, such as Fe_2O_3, start to appear in the X-ray diffraction pattern.

Electron diffraction (ED) patterns of the decomposition product were indexed in a hexagonal lattice with the unit cell parameters $a \approx 2.9$ and $c \approx 11.2$ Å (Figure 7a, left). The

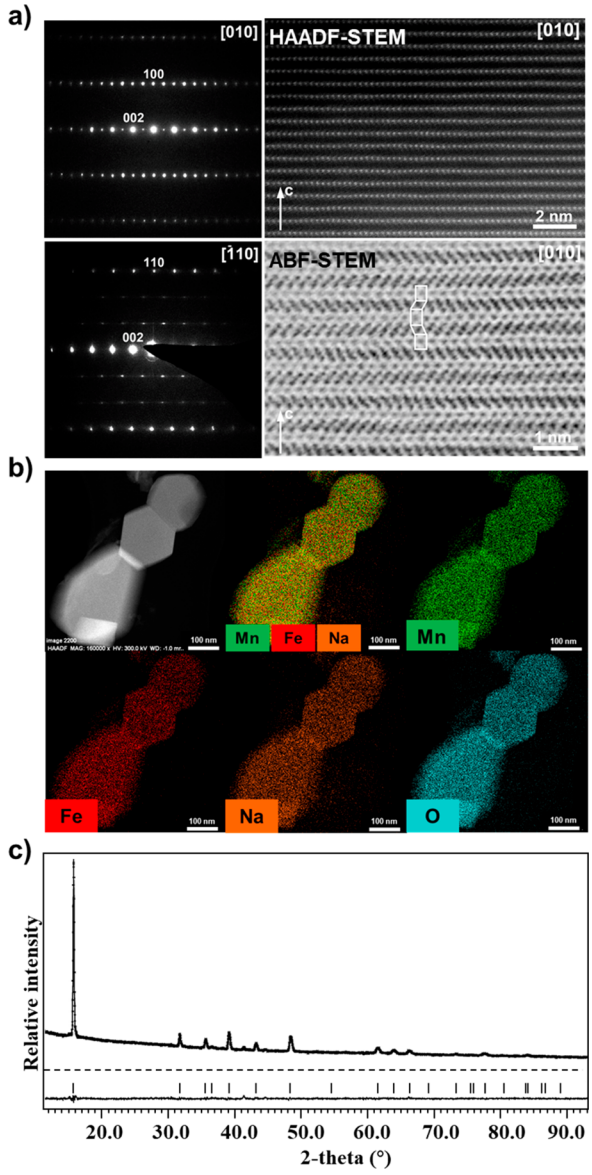

Figure 7. (a) Electron diffraction patterns of the decomposition product (left) and HAADF-STEM and ABF-STEM images of $Na_xMn_{2/3}Fe_{1/3}O_2$ (right). The sequence of the [$Na_{1-x}O_6$] trigonal prisms and [Mn/FeO_6] octahedra is marked in the ABF-STEM image. (b) HAADF-STEM image and the EDX elemental maps of Mn, Fe, Na, and O along with the mixed compositional map. (c) Experimental, calculated, and difference powder X-ray diffraction profiles for $Na_{0.48}Mn_{2/3}Fe_{1/3}O_2$ after the Rietveld refinement.

reflection condition *hhl*, $l = 2n$ corroborates the $P6_3/mmc$ space group characteristic of the P2 stacking sequence, consisting of alternating layers of the [$Na_{1-x}O_6$] trigonal prisms and [Mn/FeO_6] octahedra. Weak extra reflections in the *hhl*, $h = \pm 1/3, \pm 2/3$ reciprocal lattice rows of the [-110] ED pattern originate, most probably, from partial local ordering of Na ions and cation vacancies. The P2 stacking sequence has been confirmed by observations of the crystal structure with aberration-corrected high-angle annular dark-field scanning transmission electron microscopy (HAADF-

https://dx.doi.org/10.1021/jacs.0c05139
J. Am. Chem. Soc. 2020, 142, 12767−12776

STEM) and annular bright-field STEM (ABF-STEM; Figure 7a, right). Bright dots in the [010] HAADF-STEM image denote the Mn/Fe columns, which demonstrate no lateral shift as expected for the P2 stacking (in contrast to the O3 stacking, where the adjacent layers are shifted by 1/3 of the interdot distance). ABF-STEM enables the visualization of the oxygen sublattice, which allows direct tracking of the sequence of the $[Na_{1-x}O_6]$ trigonal prisms and $[Mn/FeO_6]$ octahedra.

Energy dispersive X-ray (EDX) analysis of the residue revealed highly homogeneous distribution of three metals (Figure 7b) with the Na:Mn:Fe = 0.50(3):0.64(2):0.36(3). Crystal structure of the target oxide has been solved from the X-ray powder diffraction data. Rietveld refinement confirmed the P2-type structure (Figure 7c and SI, Tables S20−S22) and revealed the Na content corresponding to the $Na_{0.48}Mn_{2/3}Fe_{1/3}O_2$ formula, in excellent agreement with the EDX analysis, as well as the TGA investigation of the $Na_{2/3}Mn_{2/3}Fe_{1/3}O_2$ residue obtained at 450 °C (SI, Figure S17b).

CONCLUSIONS

This work primarily contributes to answering an important question: can one make a hetero*multi*metallic precursor with any given metal ratio? Our research is showing that while that is certainly possible, it still requires many things to click into place. As we have shown in this study, even making a hetero*tri*metallic compound with complex M:M′:M″ ratio of 2:2:1 and featuring two neighboring elements on the Periodic Table demands an appropriate precursor structure that can be modified by a rational design strategy. The latter implies that a number of factors should be taken into account, such as imposing a sufficient difference in coordination environments of similar metals, accounting for redox behavior, and selecting ligands with specific coordination modes, steric and electronic properties. The next step is to develop an efficient, one-pot synthetic procedure that yields heterometallic complex on a large scale using commercially/readily available reagents. Another important problem is thorough characterization of heterometallic molecules that demands the employment of a combination of advanced techniques. Those should unambiguously identify the metal positions and oxidation states as well as ensure that the bulk material represents a genuine single-source rather than a multi-source precursor. Finally, the precursor should be capable of producing the phase-pure target material upon thermal decomposition.

Importantly, the hetero*tri*metallic molecular precursor $\{[Mn^{II}(ptac)_3]$-Na-$[Fe^{III}(acac)_3]$-Na-$[Mn^{II}(ptac)_3]\}$ (**3**) featuring three crystallographically independent transition metal positions not only represents the model for other similar complexes with different M^{II}/M'^{III} combinations, but it could also be utilized in the development of even more challenging hetero*tetra*metallic precursors for quinary $Na_2MM'M''O_6$ materials.

ASSOCIATED CONTENT

Supporting Information

The Supporting Information is available free of charge at https://pubs.acs.org/doi/10.1021/jacs.0c05139.

Experimental details, synthesis, X-ray powder diffraction patterns, crystal growth conditions, X-ray crystallographic procedures, synchrotron X-ray resonant diffraction and multiple-wavelength anomalous diffraction protocols, ATR-IR, DART, and Mössbauer spectra, and structural analysis of thermal decomposition products (PDF)

Additional file of crystallographic data (CIF)

AUTHOR INFORMATION

Corresponding Author

Evgeny V. Dikarev − *Department of Chemistry, University at Albany, State University of New York, Albany, New York 12222, United States;* orcid.org/0000-0001-8979-7914; Email: edikarev@albany.edu

Authors

Haixiang Han − *Department of Chemistry, University at Albany, State University of New York, Albany, New York 12222, United States; Department of Materials Science and Engineering, Cornell University, Ithaca, New York 14850, United States;* orcid.org/0000-0002-8465-9624

Jesse C. Carozza − *Department of Chemistry, University at Albany, State University of New York, Albany, New York 12222, United States*

Zheng Zhou − *Department of Chemistry, University at Albany, State University of New York, Albany, New York 12222, United States*

Yuxuan Zhang − *Department of Chemistry, University at Albany, State University of New York, Albany, New York 12222, United States*

Zheng Wei − *Department of Chemistry, University at Albany, State University of New York, Albany, New York 12222, United States*

Artem M. Abakumov − *Skolkovo Institute of Science and Technology, Moscow 143026, Russia;* orcid.org/0000-0002-7135-4629

Alexander S. Filatov − *Department of Chemistry, The University of Chicago, Chicago, Illinois 60637, United States;* orcid.org/0000-0002-8378-1994

Yu-Sheng Chen − *NSF's ChemMatCARS, Center for Advanced Radiation Source, The University of Chicago, Argonne, Illinois 60439, United States*

Daniel J. SantaLucia − *Department of Chemistry, University of Wisconsin—Madison, Madison, Wisconsin 53706, United States*

John F. Berry − *Department of Chemistry, University of Wisconsin—Madison, Madison, Wisconsin 53706, United States;* orcid.org/0000-0002-6805-0640

Complete contact information is available at: https://pubs.acs.org/10.1021/jacs.0c05139

Notes

The authors declare no competing financial interest.

ACKNOWLEDGMENTS

Financial support from the National Science Foundation is gratefully acknowledged (CHE-1955585 (E.V.D.), CHE-1919810 (thermogravimetric analyzer), and CHE-1953924 (J.F.B.)). A.A. thanks the Russian Science Foundation (Grant No. 17-73-30006). NSF's ChemMatCARS Sector 15 is principally supported by the Divisions of Chemistry (CHE) and Materials Research (DMR), National Science Foundation, under Grant No. NSF/CHE-1834750. Use of the Advanced Photon Source, an Office of Science User Facility operated for the U.S. Department of Energy (DOE) Office of Science by

Argonne National Laboratory, was supported by the U.S. DOE under Contract No. DE-AC02-06CH11357.

REFERENCES

(1) Abd-El-Aziz, A. S.; Strohm, E. A. Transition Metal-Containing Macromolecules: En Route to New Functional Materials. *Polymer* **2012**, *53*, 4879−4921.

(2) Greiner, M. T.; Chai, L.; Helander, M. G.; Tang, W.-M.; Lu, Z.-H. Transition Metal Oxide Work Functions: The Influence of Cation Oxidation State and Oxygen Vacancies. *Adv. Funct. Mater.* **2012**, *22*, 4557−4568.

(3) Ling, T.; Zhang, T.; Ge, B.; Han, L.; Zheng, L.; Lin, F.; Xu, Z.; Hu, W.-B.; Du, X.-W.; Davey, K.; Qiao, S.-Z. Well-Dispersed Nickel- and Zinc-Tailored Electronic Structure of a Transition Metal Oxide for Highly Active Alkaline Hydrogen Evolution Reaction. *Adv. Mater.* **2019**, *31*, 1807771.

(4) Dou, S.; Wang, X.; Wang, S. Rational Design of Transition Metal-Based Materials for Highly Efficient Electrocatalysis. *Small Methods* **2019**, *3*, 1800211.

(5) Mackus, A. J. M.; Schneider, J. R.; MacIsaac, C.; Baker, J. G.; Bent, S. F. Synthesis of Doped, Ternary, and Quaternary Materials by Atomic Layer Deposition: A Review. *Chem. Mater.* **2019**, *31*, 1142−1183.

(6) Huang, Y.-Y.; Lin, L.-Y. Synthesis of Ternary Metal Oxides for Battery-Supercapacitor Hybrid Devices: Influences of Metal Species on Redox Reaction and Electrical Conductivity. *ACS Appl. Energy Mater.* **2018**, *1*, 2979−2990.

(7) Halder, L.; Maitra, A.; Das, A. K.; Bera, R.; Karan, S. K.; Paria, S.; Bera, A.; Si, S. K.; Khatua, B. B. Fabrication of an Advanced Asymmetric Supercapacitor Based on Three-Dimensional Copper−Nickel−Cerium−Cobalt Quaternary Oxide and GNP for Energy Storage Application. *ACS Appl. Electron. Mater.* **2019**, *1*, 189−197.

(8) Kraytsberg, A.; Ein-Eli, Y. Higher, Stronger, Better··· A Review of 5 V Cathode Materials for Advanced Lithium-Ion Batteries. *Adv. Energy Mater.* **2012**, *2*, 922−939.

(9) Kweon, H.-J.; Kim, G. B.; Lim, H. S.; Nam, S. S.; Park, D. G. Synthesis of $Li_xNi_{0.85}Co_{0.15}O_2$ by the PVA-Precursor Method and Charge-Discharge Characteristics of a Lithium Ion Battery Using This Material as Cathode. *J. Power Sources* **1999**, *83*, 84−92.

(10) Yuan, D. D.; Wang, Y. X.; Cao, Y. L.; Ai, X. P.; Yang, H. X. Improved Electrochemical Performance of Fe-Substituted $NaNi_{0.5}Mn_{0.5}O_2$ Cathode Materials for Sodium-Ion Batteries. *ACS Appl. Mater. Interfaces* **2015**, *7*, 8585−8591.

(11) Yada, C.; Ohmori, A.; Ide, K.; Yamasaki, H.; Kato, T.; Saito, T.; Sagane, F.; Iriyama, Y. Dielectric Modification of 5V-Class Cathodes for High-Voltage All-Solid-State Lithium Batteries. *Adv. Energy Mater.* **2014**, *4*, 1301416.

(12) Hwang, J.-Y.; Myung, S.-T.; Sun, Y.-K. Sodium-Ion Batteries: Present and Future. *Chem. Soc. Rev.* **2017**, *46*, 3529−3614.

(13) Schaak, R. E.; Sra, A. K.; Leonard, B. M.; Cable, R. E.; Bauer, J. C.; Han, Y.-F.; Means, J.; Teizer, W.; Vasquez, Y.; Funck, E. S. Metallurgy in a Beaker: Nanoparticle Toolkit for the Rapid Low-Temperature Solution Synthesis of Functional Multimetallic Solid-State Materials. *J. Am. Chem. Soc.* **2005**, *127*, 3506−3515.

(14) Yabuuchi, N.; Kubota, K.; Dahbi, M.; Komaba, S. Research Development on Sodium-Ion Batteries. *Chem. Rev.* **2014**, *114*, 11636−11682.

(15) Bensalah, N.; Dawood, H. Review on Synthesis, Characterizations, and Electrochemical Properties of Cathode Materials for Lithium Ion Batteries. *J. Mater. Sci. Eng.* **2016**, *5*, 258.

(16) Croguennec, L.; Palacin, M. R. Recent Achievements on Inorganic Electrode Materials for Lithium-Ion Batteries. *J. Am. Chem. Soc.* **2015**, *137*, 3140−3156.

(17) Han, M. H.; Gonzalo, E.; Singh, G.; Rojo, T. A Comprehensive Review of Sodium Layered Oxides: Powerful Cathodes for Na-Ion Batteries. *Energy Environ. Sci.* **2015**, *8*, 81−102.

(18) Yoon, Y. K.; Park, C. W.; Ahn, H. Y.; Kim, D. H.; Lee, Y. S.; Kim, J. Synthesis and Characterization of Spinel Type High-Power Cathode Materials $LiM_xMn_{2-X}O_4$ (M = Ni, Co, Cr). *J. Phys. Chem. Solids* **2007**, *68*, 780−784.

(19) Xu, J.; Chou, S.-L.; Gu, Q.-f.; Liu, H.-K.; Dou, S.-X. The Effect of Different Binders on Electrochemical Properties of $LiNi_{1/3}Mn_{1/3}Co_{1/3}O_2$ Cathode Material in Lithium Ion Batteries. *J. Power Sources* **2013**, *225*, 172−178.

(20) Cho, S.-J.; Chung, C.-C.; Podowitz-Thomas, S.; Jones, J. L. Understanding the Lithium Deficient $Li_xNi_yMn_zCo_{1-Y-Z}O_2$ $(x < 1)$ Cathode Materials Structure. *Mater. Chem. Phys.* **2019**, *228*, 32−36.

(21) Jung, S.-K.; Gwon, H.; Hong, J.; Park, K.-Y.; Seo, D.-H.; Kim, H.; Hyun, J.; Yang, W.; Kang, K. Understanding the Degradation Mechanisms of $LiNi_{0.5}Co_{0.2}Mn_{0.3}O_2$ Cathode Material in Lithium Ion Batteries. *Adv. Energy Mater.* **2014**, *4*, 1300787.

(22) Wei, Z.; Filatov, A. S.; Dikarev, E. V. Volatile Heterometallic Precursors for the Low-Temperature Synthesis of Prospective Sodium Ion Battery Cathode Materials. *J. Am. Chem. Soc.* **2013**, *135*, 12216−12219.

(23) Lee, E.; Brown, D. E.; Alp, E. E.; Ren, Y.; Lu, J.; Woo, J.-J.; Johnson, C. S. New Insights into the Performance Degradation of Fe-Based Layered Oxides in Sodium-Ion Batteries: Instability of Fe^{3+}/Fe^{4+} Redox in α-$NaFeO_2$. *Chem. Mater.* **2015**, *27*, 6755−6764.

(24) Nguyen, N.-A.; Kim, K.; Choi, K. H.; Jeon, H.; Lee, K.; Ryou, M.-H.; Lee, Y. M. Effect of Calcination Temperature on a P-Type $Na_{0.6}Mn_{0.65}Ni_{0.25}Co_{0.10}O_2$ Cathode Material for Sodium-Ion Batteries. *J. Electrochem. Soc.* **2017**, *164*, A6308−A6314.

(25) Yoncheva, M.; Stoyanova, R.; Zhecheva, E.; Kuzmanova, E.; Sendova-Vassileva, M.; Nihtianova, D.; Carlier, D.; Guignard, M.; Delmas, C. Structure and Reversible Lithium Intercalation in a New P′3-Phase: $Na_{2/3}Mn_{1-y}Fe_yO_2$ $(y = 0, 1/3, 2/3)$. *J. Mater. Chem.* **2012**, *22*, 23418−23427.

(26) Zhao, J.; Zhao, L.; Dimov, N.; Okada, S.; Nishida, T. Electrochemical and Thermal Properties of α-$NaFeO_2$ Cathode for Na-Ion Batteries. *J. Electrochem. Soc.* **2013**, *160*, A3077−A3081.

(27) Han, H.; Wei, Z.; Barry, M. C.; Carozza, J. C.; Alkan, M.; Rogachev, A. Yu.; Filatov, A. S.; Abakumov, A. M.; Dikarev, E. V. A Three Body Problem: A Genuine Hetero*tri*metallic Molecule vs. A Mixture of Two Parent Hetero*bi*metallic Molecules. *Chem. Sci.* **2018**, *9*, 4736−4745.

(28) Sharma, G.; Kumar, D.; Kumar, A.; Al-Muhtaseb, A. H.; Pathania, D.; Naushad, M.; Mola, G. T. Revolution from Monometallic to Trimetallic Nanoparticle Composites, Various Synthesis Methods and Their Applications: A Review. *Mater. Sci. Eng., C* **2017**, *71*, 1216−1230.

(29) Kodera, T.; Ogihara, T. Synthesis and Electrochemical Properties of $Na_{2/3}Fe_{1/3}Mn_{2/3}O_2$ Cathode Materials for Sodium Ion Battery by Spray Pyrolysis. *J. Ceram. Soc. Jpn.* **2014**, *122*, 483−487.

(30) Mortemard de Boisse, B. *Structural and Electrochemical Studies of $Na_xMn_{1-y}Fe_yO_2$ and $NaNiO_2$ Materials as Positive Electrode for Na-Ion Batteries*. Ph.D. Thesis; Université de Bordeaux, 2014.

(31) Sénateur, J. P.; Dubourdieu, C.; Weiss, F.; Rosina, M.; Abrutis, A. Pulsed Injection MOCVD of Functional Electronic Oxides. *Adv. Mater. Opt. Electron.* **2000**, *10*, 155−161.

(32) Lin, P. A.; Sankaran, R. M. Plasma-Assisted Dissociation of Organometallic Vapors for Continuous, Gas-Phase Preparation of Multimetallic Nanoparticles. *Angew. Chem., Int. Ed.* **2011**, *50*, 10953−10956.

(33) Navulla, A.; Huynh, L.; Wei, Z.; Filatov, A. S.; Dikarev, E. V. Volatile Single-Source Molecular Precursor for the Lithium Ion Battery Cathode. *J. Am. Chem. Soc.* **2012**, *134*, 5762−5765.

(34) Lu, H.; Wright, D. S.; Pike, S. D. The Use of Mixed-Metal Single Source Precursors for the Synthesis of Complex Metal Oxides. *Chem. Commun.* **2020**, *56*, 854−871.

(35) Han, H.; Carozza, J. C.; Colliton, A. P.; Zhang, Y.; Wei, Z.; Filatov, A. S.; Chen, Y.-S.; Alkan, M.; Rogachev, A. Yu.; Dikarev, E. V. Hetero*tri*metallic Mixed-Valent Molecular Precursors Containing Periodic Table Neighbors: Assignment of Metal Positions and Oxidation States. *Angew. Chem.* **2020**, *132*, 9711−9717.

(36) Song, J.; Wang, L.; Lu, Y.; Liu, J.; Guo, B.; Xiao, P.; Lee, J.-J.; Yang, X.-Q.; Henkelman, G.; Goodenough, J. B. Removal of

https://dx.doi.org/10.1021/jacs.0c05139
J. Am. Chem. Soc. 2020, 142, 12767−12776

Interstitial H_2O in Hexacyanometallates for a Superior Cathode of a Sodium-Ion Battery. *J. Am. Chem. Soc.* **2015**, *137*, 2658−2664.
(37) Blair, V. L.; Carrella, L. M.; Clegg, W.; Klett, J.; Mulvey, R. E.; Rentschler, E.; Russo, L. Structural and Magnetic Insights into the Trinuclear Ferrocenophane and Unexpected Hydrido Inverse Crown Products of Alkali-Metal-Mediated Manganation(II) of Ferrocene. *Chem. - Eur. J.* **2009**, *15*, 856−863.
(38) Saha, A.; Musie, G.; Powell, D. R. Sodium Tris-(acetylacetonato-κ^2O,O')Manganese(II). *Acta Crystallogr., Sect. E: Struct. Rep. Online* **2005**, *61*, m1144−m1146.
(39) Li, M.; Yang, K.; Liu, J.; Hu, X.; Kong, D.; Liu, T.; Zhang, M.; Pan, F. A Heterobimetallic Single-Source Precursor Enabled Layered Oxide Cathode for Sodium-Ion Batteries. *Chem. Commun.* **2018**, *54*, 10714−10717.
(40) Lieberman, C. M.; Filatov, A. S.; Wei, Z.; Rogachev, A. Yu.; Abakumov, A. M.; Dikarev, E. V. Mixed-Valent, Heteroleptic Homometallic Diketonates as Templates for the Design of Volatile Heterometallic Precursors. *Chem. Sci.* **2015**, *6*, 2835−2842.
(41) Baker, T. M.; Howard, K. M.; Brennessel, W. W.; Neidig, M. L. Crystal Structure of a Third Polymorph of Tris-(acetyl-acetonato-k^2O,O')Iron(III). *Acta Crystallogr. E* **2015**, *71*, m228−m229.
(42) Han, H.; Wei, Z.; Barry, M. C.; Filatov, A. S.; Dikarev, E. V. Heterometallic Molecular Precursors for a Lithium-Iron Oxide Material: Synthesis, Solid State Structure, Solution and Gas-Phase Behaviour, and Thermal Decomposition. *Dalton Trans.* **2017**, *46*, 5644−5649.
(43) Baidina, I. A.; Kurat'eva, N. V.; Stabnikov, P. A.; Gromilov, S. A. Crystal and Molecular Structure of *Tris*-(1,1,1-trifluoro-5,5-dimethylhexan-2,4-dionato)Iron(III). *J. Struct. Chem.* **2007**, *48*, 494−499.
(44) Geremia, S.; Demitri, N. Crystallographic Study of Manganese-(III) Acetylacetonate: An Advanced Undergraduate Project with Unexpected Challenges. *J. Chem. Educ.* **2005**, *82*, 460.
(45) Freitag, R.; Conradie, J. Understanding the Jahn−Teller Effect in Octahedral Transition-Metal Complexes: A Molecular Orbital View of the Mn(β-diketonato)$_3$ Complex. *J. Chem. Educ.* **2013**, *90*, 1692−1696.
(46) Fackler, J. P.; Avdeef, A. Crystal and Molecular Structure of Tris(2,4-pentanedionato)Manganese(III), $Mn(O_2C_5H_7)_3$, a Distorted Complex as Predicted by Jahn-Teller Arguments. *Inorg. Chem.* **1974**, *13*, 1864−1875.
(47) Hodeau, J.-L.; Favre-Nicolin, V.; Bos, S.; Renevier, H.; Lorenzo, E.; Berar, J.-F. Resonant Diffraction. *Chem. Rev.* **2001**, *101*, 1843−1868.
(48) Han, H.; Wei, Z.; Filatov, A. S.; Carozza, J. C.; Alkan, M.; Rogachev, A. Yu.; Shevtsov, A.; Abakumov, A. M.; Pak, C.; Shatruk, M.; Chen, Y. S.; Dikarev, E. V. Three to Tango Requires a Site-Specific Substitution: Hetero*tri*metallic Molecular Precursors for High-Voltage Rechargeable Batteries. *Chem. Sci.* **2019**, *10*, 524−534.
(49) Lieberman, C. M.; Barry, M. C.; Wei, Z.; Rogachev, A. Yu.; Wang, X.; Liu, J.-L.; Clérac, R.; Chen, Y.-S.; Filatov, A. S.; Dikarev, E. V. Position Assignment and Oxidation State Recognition of Fe and Co Centers in Heterometallic Mixed-Valent Molecular Precursors for the Low-Temperature Preparation of Target Spinel Oxide Materials. *Inorg. Chem.* **2017**, *56*, 9574−9584.
(50) Yabuuchi, N.; Kajiyama, M.; Iwatate, J.; Nishikawa, H.; Hitomi, S.; Okuyama, R.; Usui, R.; Yamada, Y.; Komaba, S. P2-Type $Na_x[Fe_{1/2}Mn_{1/2}]O_2$ Made from Earth-Abundant Elements for Rechargeable Na batteries. *Nat. Mater.* **2012**, *11*, 512−517.
(51) Zhao, J.; Xu, J.; Lee, D. H.; Dimov, N.; Meng, Y. S.; Okada, S. Electrochemical and Thermal Properties of P2-Type $Na_{2/3}Fe_{1/3}Mn_{2/3}O_2$ for Na-Ion Batteries. *J. Power Sources* **2014**, *264*, 235−239.

https://dx.doi.org/10.1021/jacs.0c05139
J. Am. Chem. Soc. 2020, 142, 12767−12776